Interplay between spin dynamics and crystal field in the multiferroic compound $HoMnO_3$

X. Fabrèges,[1] S. Petit,[1] J.-B. Brubach,[2] P. Roy,[2] M. Deutsch,[2,*] A. Ivanov,[3] L. Pinsard-Gaudart,[4] V. Simonet,[5] R. Ballou,[5] and S. de Brion[5,†]

[1]*Laboratoire Léon Brillouin, CEA, CNRS, Université Paris-Saclay, CE-Saclay, F-91191 Gif sur Yvette, France*
[2]*Synchrotron SOLEIL, L'Orme des Merisiers Saint-Aubin, 91192 Gif sur Yvette, France*
[3]*Institut Laue-Langevin, 71 avenue des Martyrs CS 20156, 38042 Grenoble Cedex 9, France*
[4]*SP2M-ICMMO, UMR-CNRS 8182, Université Paris-Sud, Université Paris-Saclay, 91405 Orsay, France*
[5]*Université Grenoble Alpes, CNRS, Institut Néel, 38000 Grenoble, France*

(Received 1 February 2019; revised manuscript received 6 August 2019; published 23 September 2019)

In the multiferroic hexagonal manganite $HoMnO_3$, inelastic neutron scattering and synchrotron-based THz spectroscopy have been used to investigate the spin waves associated with the Mn order together with Ho crystal-field excitations. While the Mn order sets in first below 80 K, a spin reorientation occurs below 37 K, a rare feature in the rare-earth manganites. We show that several Ho crystal-field excitations are present in the same energy range as the magnons, and that they are all affected by the spin reorientation. Moreover, several anomalous features are observed in the excitations at low temperature. Our analysis and calculations for the Mn spin waves and Ho crystal-field excitations suggest Mn-Ho coupling mechanisms as well as electric charge redistribution affecting the dynamics.

DOI: 10.1103/PhysRevB.100.094437

I. INTRODUCTION

Multiferroics continue to attract much attention in condensed-matter physics because of the promising applications in spintronics they offer, but also because these materials raise fundamental questions. One of these concerns the understanding of the microscopic origin of the coupling between magnetic and electric degrees of freedom, and how new excitations resulting from this coupling, for instance electromagnons, can emerge. Electromagnons were first reported in 2006 as magnetic excitations excitable by the electric field component of the electromagnetic wave [1]. Since then, electromagnons have been observed in several compounds with noncollinear magnetic order, such as perovskites [1,2], hexaferrites [3], or even the more simple cupric oxide [4]. Various mechanisms at the origin of these excitations were invoked and identified, among which are the inverse Dzyaloshinskii-Moriya interaction [5], *p-d* hybridization [6], the symmetric exchange-striction mechanism [7] or higher harmonics of the magnetic cycloids [8]. Other types of excitations involving electric and magnetic degrees of freedom have also been reported, such as atomic rotation mode excited by the magnetic field component of the terahertz (THz) light [9], or hybrid excitations arising from the interplay between rare-earth crystal field (CF) excitations and 3*d* transition-metal magnons [10,11], in particular in the hexagonal manganite $ErMnO_3$ [12]. All these hybrid excitations often lie in the THz range, and they are also investigated using inelastic neutron [13] or x-ray scattering [14] and Raman spectroscopy [15].

The hexagonal manganites *h*-$RMnO_3$, where R = Y, Er, Ho, etc., crystallizing in the $P6_3cm$ space group, have been widely studied [16–19] since they combine remarkable properties associated with multiferroism and magnetic frustration. They belong to type I multiferroics, where ferroelectricity and magnetic orders occur at different temperatures: the onset of an electric polarization along the *c*-axis at much higher temperature ($T_C \simeq 800$ K) than the ordering of the Mn magnetic moments ($T_N \simeq 80$ K). Despite these different energy scales, non-negligible coupling between the electric and magnetic degrees of freedom is present. For instance, the Mn magnetic ordering is accompanied by ionic motions inside the unit cell [20,21], giving rise to a giant magnetoelastic coupling, connected with an increase of the ferroelectric polarization. The Mn sublattice consists of triangular planes (Fig. 1) with a peculiar stacking along the *c*-axis, each Mn^{3+} ion sitting close to the middle of the triangle of Mn^{3+} belonging to adjacent layers. The actual materials then share a 120° spin structure for the Mn magnetic moments in the triangular planes, but the stacking and relative phase difference of these patterns depend on the R atom (magnetic R = Ho, Yb, ... or not R = Y, Sc), and correspond to the four one-dimensional irreducible representations shown in Fig. 1. A key parameter tuning the sign of the exchange interaction and the Mn^{3+} single-ion anisotropy seems to be the shift away from 1/3 of the x position of the Mn^{3+} ions within the triangular plane [20,22]. The ions R^{3+} are situated on two Wyckoff sites 2*a* and 4*b*. For magnetic rare earths, they also order at lower temperature, either polarized by the Mn molecular field (site 4*b*) or from their mutual interaction in a temperature range of a few K (site 2*a*) [23,24].

In this study, we focus on the Ho compound, which has been studied intensively for its rich H-T phase diagram and its strong magnetoelectric effects [18,25]. It becomes

*Université de Lorraine, CNRS, CRM2, F-54000 Nancy, France.
†sophie.debrion@neel.cnrs.fr

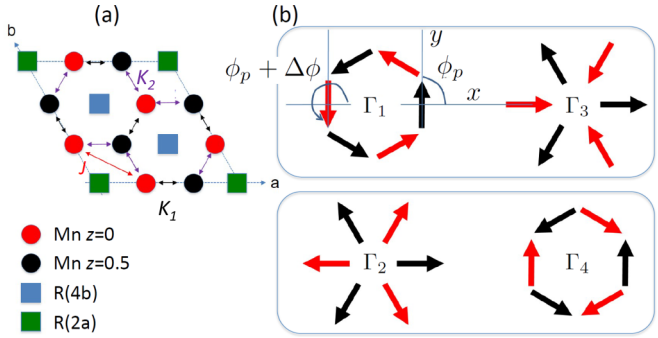

FIG. 1. Sketch of the $R\mathrm{MnO_3}$ crystallographic and magnetic structures. (a) Projection of the different atomic positions onto the *ab*-plane, omitting the oxygens for clarity. The Mn ions on the 6*c* Wyckoff site have an x coordinate within the *ab*-plane close to 1/3 and a z coordinate along the *c*-axis equal to 0 (red spheres) or 1/2 (black spheres). The rare-earths occupy two different Wyckoff sites (2*a* and 4*b*). The main intraplane (J) and interlayer ($K_{1,2}$) exchange interactions between the Mn magnetic moments are indicated. (b) Magnetic arrangement of the Mn ions with zero propagation vector corresponding to the four one-dimensional irreducible representations Γ_i of the $P6_3cm$ space group. The homometric pairs, indistinguishable through neutron scattering if $x_{\mathrm{Mn}} = 1/3$, are indicated by the boxes. x is along the *a*-axis, y is perpendicular to it in the *ab*-plane, and z is along the *c*-axis. ϕ_p and $\Delta\phi$ are, respectively, the angle of the magnetic moment in the p plane and the dephasing of this spin with respect to the corresponding one in the adjacent plane.

ferroelectric at 875 K, and the Mn magnetic moments order at $T_N = 75$ K in the Γ_4 representation (see Fig. 1). Remarkably, a spin reorientation occurs at $T_{\mathrm{SR}} = 37$ K, toward the Γ_3, which is concomitant with the ordering of the Ho(4*b*) magnetic moments, while the Ho(2*a*) moments order around $T_{\mathrm{Ho}} = 5$ K, both along the *c*-axis [20,26–30]. This Mn reorientation transition, unique in the hexagonal manganites, shows up also in the electric properties with a drop in the electric polarization below T_{SR}, which is further recovered at T_{Ho} [31]. Signatures of the rare-earth Mn coupling in the spin dynamics in an applied magnetic field have also been reported [32,33], although no rare-earth CF-Mn magnon hybridization has yet been observed.

We report here a detailed study on the dynamical properties of this compound in the THz range using both electromagnetic waves and neutrons as complementary probes. We show that the THz dynamics is particularly complex in $\mathrm{HoMnO_3}$ due to the presence of several Ho CF excitations in addition to the Mn spin waves that surprisingly become nondispersive along the *c*-axis at low temperature. To interpret the observed spectra and their remarkable temperature dependence through the spin reorientation transition and below, we have performed calculations both for Mn and Ho dynamics. Our work brings new insight into the complex spin dynamics of this compound, including possible signatures of the couplings between the different magnetic ions, but also with their charge surroundings.

II. EXPERIMENTAL DETAILS

Single crystals have been grown using the floating zone method, yielding rods of about 7 mm in diameter and 4 cm long. From these crystals, two small plaquettes were cut for the THz measurements (typically 2 mm in diameter and 300 μm in thickness): one with the *c*-axis perpendicular to the plaquette, the other with the *c*-axis within the plaquette. The polarized THz emission of the synchrotron at SOLEIL was used to probe the THz properties, similarly to the study on $\mathrm{ErMnO_3}$ [12].

Inelastic neutron-scattering (INS) measurements were performed at the thermal spectrometer IN8 (ILL) as well as at the 4F1 and 4F2 cold triple-axis spectrometers installed at LLB. The final wave vector used was $k_f = 2.662$, 1.55, or 1.3 $\mathrm{Å}^{-1}$ depending on the desired energy resolution (0.8, 0.25, and 0.12 meV, respectively). Higher-order reflections were removed using a PG (IN8) or nitrogen-cooled beryllium filter (4F). The sample was mounted to have access to $Q = (h, 0, \ell)$ scattering wave vectors and attached to the cold finger of an orange cryostat. Several energy scans taken along $Q = (h, 0, \ell)$ were collected to construct the maps shown in Figs. 2 and 8.

III. INELASTIC NEUTRON SCATTERING

The Mn spin-wave spectra in $R\mathrm{MnO_3}$ materials have been studied in great detail by means of inelastic neutron scattering [13,20,23,34–38] (see also Appendix A 1 and Fig. 8). Branches, dispersing in the *ab*-plane and much less along the *c*-axis, have been observed, allowing us to determine the amplitude of the Mn-Mn magnetic interactions. Here, however, we pursue a different objective. We focus on the low-energy sector, aiming at unraveling the interplay between those modes and the low-energy Ho crystal-field excitations. Figure 2 gives an overview of our results. Panel (a) shows the weak dispersions along $\mathbf{c}^*$ at different temperatures, while panel (b) shows the temperature dependence taken at the zone centers (1, 0, 0) and (1, 0, 1).

We first observe a roughly flat feature, labeled M, at about $\Delta = 45\ \mathrm{cm}^{-1}$ at low temperatures. According to prior studies, it can be unambiguously attributed to a Mn spin wave branch (see the Appendix A 1). Along $\mathbf{c}^*$, it looks like a flat band, due to the weakness of the interplane couplings. As shown in panel (b), Δ softens with increasing temperature as expected.

The second remarkable feature, labeled M', is a dispersive branch corresponding also to a Mn spin wave. Above T_{SR}, its structure factor is large at (1,0,0), as expected for Γ_4 magnetic structure. Quite strikingly, below T_{SR}, this large spectral weight is transferred to (1,0,1), as a result of the transition to Γ_3 [20]. This change of the spectral weight can also be noticed in panel (b). The amplitude of dispersion of M' actually depends on the small differences that exist between different exchange paths (see Appendix A 1). Finally, this branch shows a finite gap, due to small single-ion anisotropies of the $\mathrm{Mn^{3+}}$, which forces the spin to point along the x or y axis (see Fig. 1). An additional origin of this anisotropy might arise from the Ho molecular field, and it leads to a gap proportional to the Ho(4*b*) ordered moment. Indeed, at the mean-field level, the coupling between the 3*d* and 4*f* magnetic species reads

$$\mathcal{V} = \sum_{m,i,p,\ell} \mathbf{S}_{m,i}\, g_{m,i,p,\ell}\, \langle \mathbf{J}_{p,\ell} \rangle, \qquad (1)$$

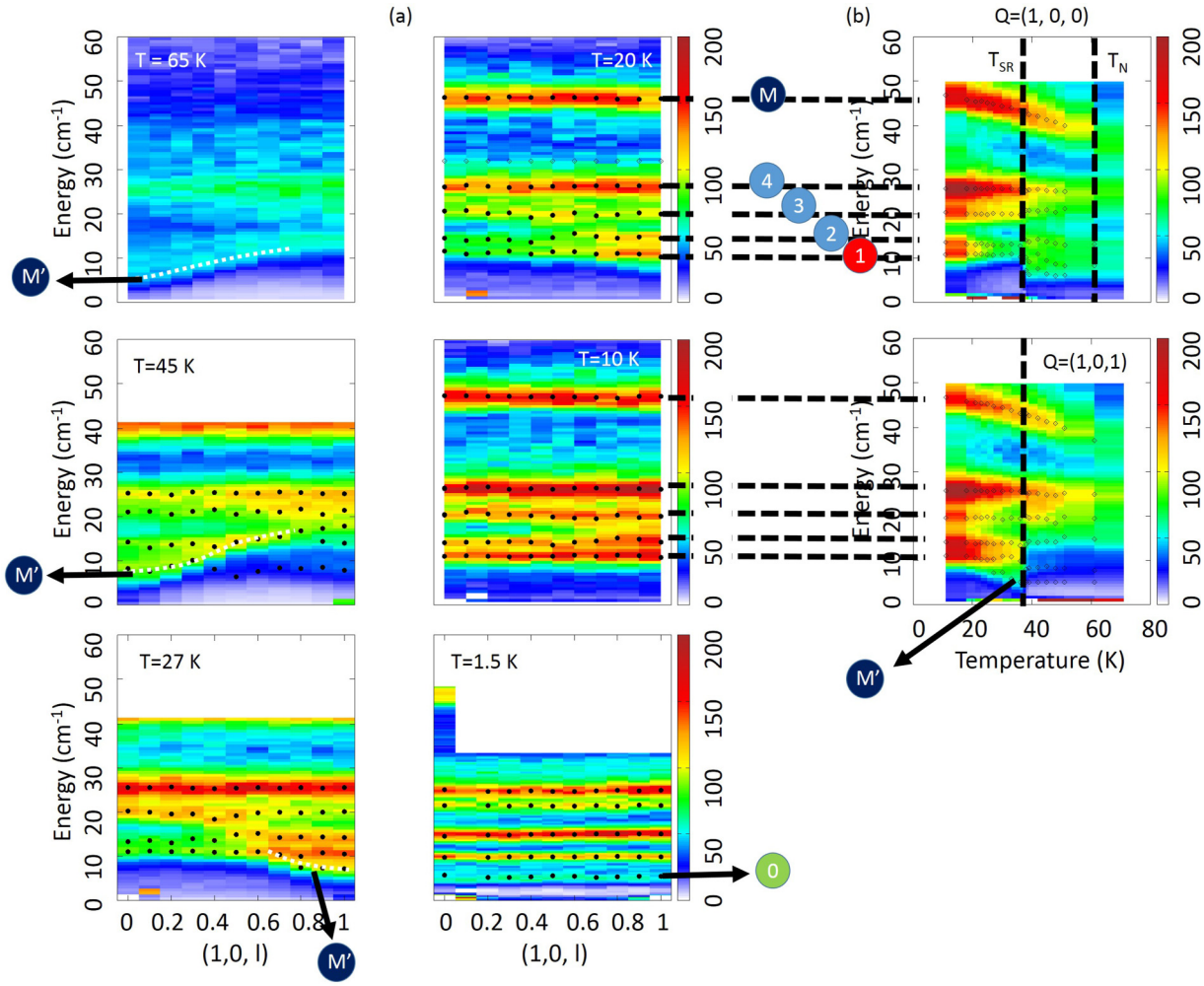

FIG. 2. Inelastic neutron-scattering color maps in $HoMnO_3$ obtained gathering several constant-Q energy scans corrected for the detailed balance factor. Vertical bars give the neutron counts in arbitrary units. The dots added on the color maps were obtained by Gaussian fits of the individual scans. (a) Maps for the $(1, 0, \ell)$ reciprocal space direction at different temperatures, ranging from 65 K down to 1.5 K. The spin reorientation occurs at $T_{SR} = 37$ K. The upper spin-wave branch (labeled M) associated with Mn order is observed around 45 cm^{-1}. The lower branch (M') can be observed at 65, 45, and 27 K. The dashed white lines are guide to the eyes. The spectral weight is typical of the Γ_4 configuration at 65 and 45 K, but it becomes typical of Γ_3 at 27 K. In addition, flat modes (0–4), likely Ho crystal-field excitations, are also observed. For the temperatures below 27 K, the spin waves gradually fade away into the CF excitations, and only nondispersive excitations remain at 1.5 K (below T_{Ho}). (b) Maps for the (1,0,0) and (1,0,1) reciprocal space positions as a function of temperature. The dashed vertical lines indicate the transition temperatures.

where g is the coupling tensor, and m, p and i, ℓ are indices that label the unit cell and the atom for the 3d and rare-earth sublattices, respectively. $\langle \mathbf{J}_{p,\ell} \rangle$ is the average magnetic moment at the rare-earth site. It is worth noting that Ho and Mn ordered magnetic moments below T_{SR} are orthogonal. This suggests that, in the Mn-Ho coupling Hamiltonian of Eq. (1), the coupling tensor g shows nondiagonal terms, as is the case, for instance, for the pseudodipolar, the Dzyaloshinskii-Moriya interaction [39], or the highest-order trigonal anisotropy [40]. $\mathcal{V}$ polarizes the Mn spins, hence it plays the role of anisotropy. This effect is likely at play, for instance, in $YbMnO_3$ [39]. However, in the present case the expected scaling seems not to fully operate.

In addition to those spin waves, nondispersive excitations are visible, labeled 0–4. They correspond to a transition between CF levels of the two Ho^{3+} ions on 4b and 2a sites. Those labels are also used to describe the THz data presented in the next part. Note that the line labeled 0 appears at very low temperature only, hence it is probably due to the Ho ordering on site 2a. Panel (b) of Fig. 2 shows the temperature dependence of these CF transition modes. Their intensity increases gradually with decreasing temperature while their position changes slightly, but the most remarkable feature is the formation of the additional line labeled 1 just below T_{SR}. Moreover, and quite strikingly, the dispersion of M' eventually merges gradually below T_{SR} into those CF lines (at least into those below 30 cm^{-1}). Finally, the spectrum encompasses only flat bands below ≈10 K. This very peculiar temperature evolution of M' whose dispersion flattens could be attributed to a decrease of the interplane interactions as a consequence of the shift of the oxygen position x_{Mn} toward 1/3 (see the Appendix A 1) [20]. Another explanation involves hybridiza-

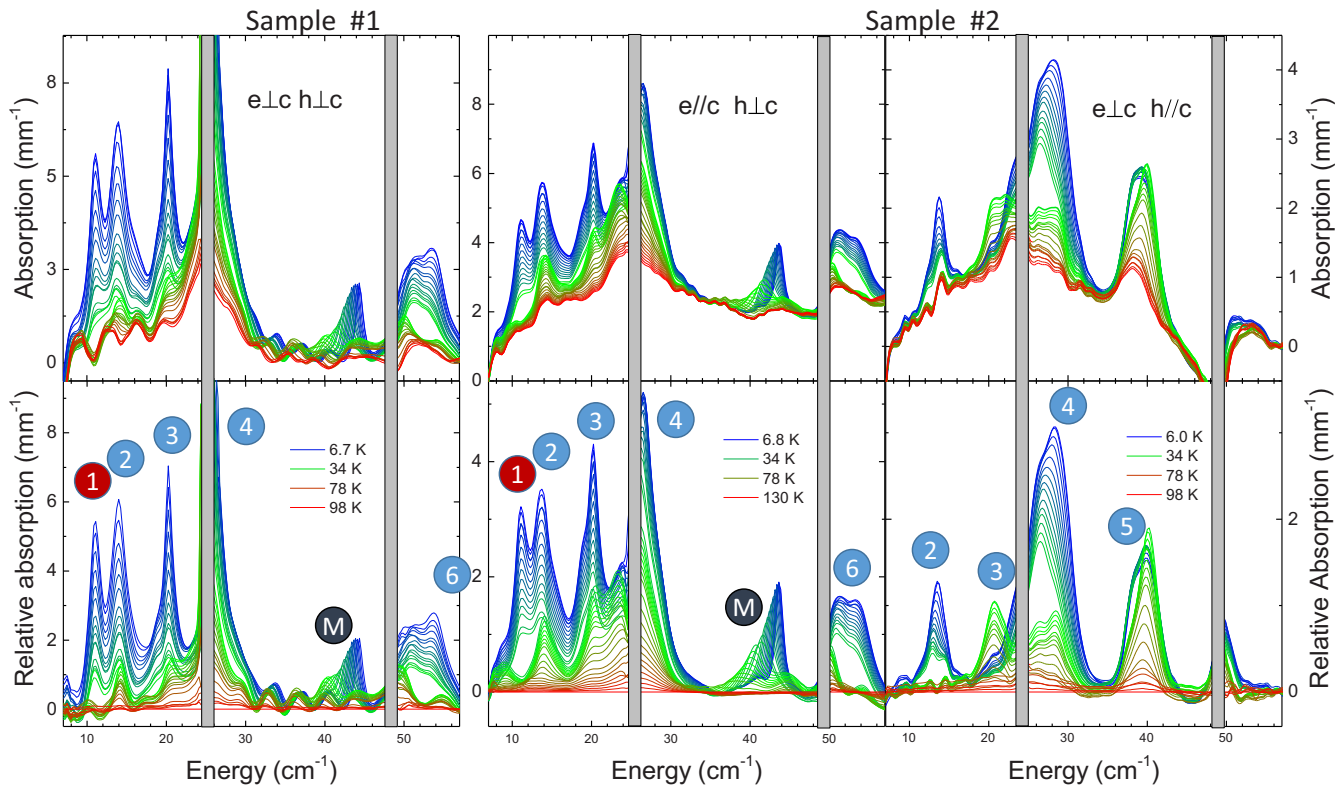

FIG. 3. THz absorption spectra of $HoMnO_3$ for the three different orientations of the electromagnetic wave **e**, **h** fields with respect to the crystal *c*-axis, using two different samples. Upper panels: absolute absorptions. Lower panels: relative absorptions with a reference above the magnetic ordering temperature at 98 or 130 K.

tion mechanisms (via a resonant process) between the Mn spin-wave dispersion and the Ho CF lines that it crosses at low temperature.

IV. SYNCHROTRON-BASED THz SPECTROSCOPY

To get a better insight into the spin dynamics, we have used THz spectroscopy as a complementary probe of both Mn spin waves and Ho crystal-field excitations. In this electromagnetic absorption technique, due to the high velocity of photons in the material, the measurements are considered in the long-wavelength limit, and a comparison with neutron data is therefore relevant for the (0, 0, 0) center of the Brillouin zone [9,12], keeping in mind that neutron scattering measures the imaginary part of the dynamical susceptibility that is equal to the THz absorption divided by the energy [41]. For the THz spectrum, all Ho crystal-field excitations should be present. As for the Mn spin waves, we have extended the calculations presented in the Appendix A 1 in Fig. 8 to the imaginary part of the susceptibility at the zone center (0,0,0). We noticed that the four different spin configurations Γ_i have the same signature at (0,0,0). It consists of a high-energy branch (M), expected around 45 cm^{-1} at low temperatures, which involves correlations between spin components perpendicular to the *c*-axis, and a single low-energy branch M' corresponding to spin correlations along the *c*-axis that is pushed to finite energy when some spin anisotropy is present.

The THz spectrum of $HoMnO_3$ was first studied in [32] where the Mn magnon mode M as well as several Ho crystal-field excitations were observed as a function of external magnetic field. The Mn magnon was more recently investigated under light irradiation [42], while its dependence on the Ho-Mn interaction is reported in [33]. Here, thanks to synchrotron-based spectroscopy, we are able to measure with great precision the whole spectra from 0.3 to 1.8 THz (10 to 60 cm^{-1}) that we will confront with neutron data.

All the spectra recorded at different temperatures from 130 or 98 K down to 6 K are shown in Fig. 3 for the three possible orientations (with regard to the *c*-axis) of the THz electric **e** and magnetic **h** fields. A detailed description is given in the Appendix A 2. Several absorption bands are observed from 11 up to 55 cm^{-1}, quite different from other hexagonal manganites such as $YMnO_3$ or $ErMnO_3$ [12], suggesting the influence of Ho ions in these THz spectra. Note that, for the two different THz polarizations with the same magnetic field direction $\mathbf{h} \perp \mathbf{c}$, the spectra are very similar and differ substantially from the case in which $\mathbf{h} \parallel \mathbf{c}$: this is a strong indication that all the observed THz excitations are of magnetic origin. The Mn magnon (M) is clearly observed as expected: it emerges below T_N and hardens when the temperature is lowered, reaching 43.7 cm^{-1} at 7 K. It is only excited for $\mathbf{h} \perp \mathbf{c}$ and therefore involves a spin component perpendicular to the *c*-axis, in agreement with the prediction from the spin-wave calculations. Besides the magnon M, six bands labeled 1–6 (each possibly including several excitations) are clearly visible. There is a good agreement with the neutron data of Fig. 2: at 20 K, below T_{SR}, the observed five flat bands along $(1, 0, \ell)$ in the neutron data correspond nicely to band 1–4

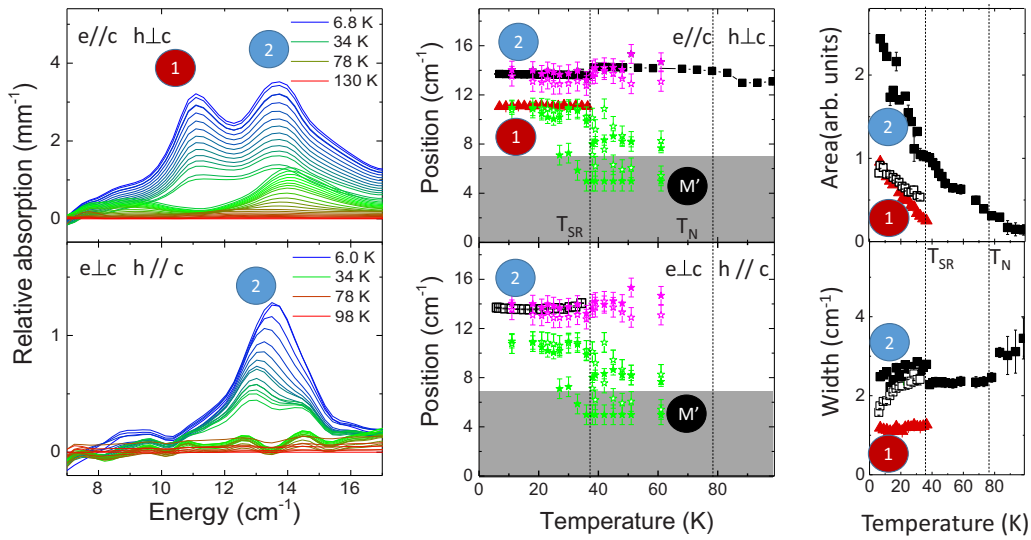

FIG. 4. Details of the THz spectra around bands 1 and 2. Left: relative absorption measured for two different orientations of **e** and **h** on the same sample. Below T_{SR}, two new excitations appear abruptly: band 1 for $\mathbf{h} \perp \mathbf{c}$ and band 2 for $\mathbf{h} \parallel \mathbf{c}$. Middle: results of the Gaussian fits for the THz absorption peak position as a function of temperature for mode 1 in red and mode 2 in black (closed and open symbols refer to $\mathbf{h} \perp \mathbf{c}$ and $\mathbf{h} \parallel \mathbf{c}$, respectively). The results from neutron measurements are also reported as open/closed star symbols for the peak positions at the $(1, 0, 0)/(1, 0, 1)$ reciprocal space position. The gray boxes correspond to the THz measurements cutoff. Right: results of Gaussian fits for the THz absorption peaks with the area and width as a function of temperature.

and to the magnon M. Band 6 is also visible as a nondispersive branch in the neutron data taken along the $(h, 0, 1)$ reciprocal space direction (see Fig. 8 in the Appendix A 1). Note that mode 5 is not visible in our neutron-scattering experiments probably because it overlaps with the magnon M or because its neutron cross section is intrinsically weak. At 45 K, above T_{SR}, five branches are visible in the neutron spectra, three of them corresponding to bands 2-3-4 in THz, while the dispersive magnon M' is not distinguishable in THz, probably because it is below the energy window of the THz spectroscopy or mixed inside bands 3-4.

The THz absorption peaks have been fitted with a Gaussian profile, and their positions in energy, spectral weight, and width are reported in Fig. 4 and in the Appendix A 2. They all show, at the reorientation transition T_{SR}, a slight change of their position in energy and a more or less pronounced change of spectral weight. The most remarkable changes can be seen in Fig. 4 where the spectra in the 7–17 cm^{-1} range are plotted: band 1 appears only below T_{SR} and for $\mathbf{h} \perp \mathbf{c}$, while band 2, always present for $\mathbf{h} \perp \mathbf{c}$, is observable only below T_{SR} when $\mathbf{h} \parallel \mathbf{c}$. Below T_{SR}, both bands are remarkably temperature-independent. The expected M' magnon in the $\mathbf{h} \parallel \mathbf{c}$ channel is not observed: above T_{SR}, according to the neutron measurements reproduced in Fig. 4, it is around 5 cm^{-1}, below 7 cm^{-1}, the THz measurement lower cutoff, while below T_{SR} it is not distinguishable from the CF excitations. As a comparison, in $ErMnO_3$, M' is observed around 18 cm^{-1} at 10 K for $\mathbf{h} \parallel \mathbf{c}$ [12]. Below T_{SR}, a more complex dynamical behavior may therefore be present in the Ho compound.

To unravel the different magnon/crystal-field contributions and their possible hybridization, we propose additional modeling of the complex Mn and Ho dynamics. We first focus on the crystal-field excitations associated with the Ho ions.

V. CRYSTAL-FIELD CALCULATIONS

Crystal-field effects were calculated in a point charge model taking into account the whole oxygen coordination shell of the Ho^{3+} ions ($4f^{10}$) for site 4*b* in C_3 symmetry and site 2*a* in C_{3v} symmetry [12,43,44]. The atomic coordinates were obtained from a refinement of neutron-diffraction data at 10 K [20]. The associated Hamiltonian for each Ho^{3+} ion in the ground multiplet $J = 8$ can be expressed as

$$H_{4b}^{CF} = A_2^0 O_2^0 + A_4^0 O_4^0 + A_4^3 O_4^3 - (A_4^3)^* O_4^{-3} + A_6^0 O_6^0 + A_6^3 O_6^3 - (A_6^3)^* O_6^{-3} + A_6^6 O_6^6 + (A_6^6)^* O_6^{-6}, \quad (2)$$

$$H_{2a}^{CF} = A_2^0 O_2^0 + A_4^0 O_4^0 + A_4^3 (O_4^3 - O_4^{-3}) + A_6^0 O_6^0 + A_6^3 (O_6^3 - O_6^{-3}) + A_6^6 (O_6^6 + O_6^{-6}) \quad (3)$$

for sites 4*b* and 2*a*, in terms of O_n^m Racah operators. A global screening factor of 20% was estimated in order to obtain the transition between the CF levels in the experimental energy range. The CF parameters resulting from this calculation, labeled set 1, are given in Table I. The deduced energy scheme is given in Fig. 5 together with the selection rules that are discussed in the Appendix A 3. For Ho 4*b*, the energy scheme contains a singlet (A) and degenerate doublets ($E_1 \bigoplus E_2$). Four different energy levels are calculated below 100 cm^{-1}. For Ho 2*a*, two singlets (A_1, A_2) and one doublet (E) are present with four different energy levels in the same energy range. They are all allowed to occur for any orientation of the THz magnetic field. The calculated absorption is shown in Figs. 6(a) and 6(b) for both orientations of the THz magnetic field **h** at 40 and 6 K, respectively. Below 60 cm^{-1}, the THz upper cutoff frequency, two CF transitions are calculated for the Ho 4*b* site, and four of them for the 2*a* site, corresponding to the observed 2–6 bands. The energy and relative intensities

TABLE I. CF parameters of sets 1 and 2 for the two Ho sites in the Racah formalism (see the text).

Set 1	Ho (4*b*)	Ho (2*a*)
A_2^0	0.392332	−0.664753
A_4^0	0.000747	−0.000978
A_4^3	$-0.037963 + i\ 0.008016$	−0.039276
A_6^0	−0.000776	−0.000848
A_6^3	$0.000337 - i\ 0.000075$	0.000219
A_6^6	−0.000492	−0.000531
Set 2	Ho (4*b*)	Ho (2*a*)
A_2^0	0.392332	−0.531802
A_4^0	0.000747	−0.000978
A_4^3	$-0.037963 + i\ 0.008016$	−0.039276
A_6^0	−0.000705	−0.000917
A_6^3	$0.000306 - i\ 0.000068$	0.000237
A_6^6	−0.000448	−0.000574

of the highest energy bands 5 and 6 are correctly reproduced. However, the agreement between the calculations and the observed complex set of mixed excitations below 30 cm^{-1} is less accurate.

To go further, we took into account the coupling of the Ho 4*b* magnetic moments with the Mn ones expected to occur below T_{SR} (discarding a possible magnetic coupling of the Ho 2*a* with Mn) [30]. This was achieved by including in the calculations the influence of the local magnetic field produced by the Mn moments on the Ho 4*b* site, similarly to the case of $ErMnO_3$ [12]. This field was chosen along the *c*-axis according to the observed *c*-direction of the Ho ordered magnetic moments. Its value was adjusted at 2 T so that the ordered Ho 4*b* magnetic moment extracted from the neutron-diffraction data is reproduced at low temperature (see the Appendix A 1). The influence of this magnetic field is to change slightly the energy of some peaks and to produce additional splitting of some CF levels [see Figs. 6(b) and 6(c) for the parameter set 1]. We can notice in particular that the lowest-energy CF peak corresponding to Ho 4*b* (in blue) in zero field splits into two peaks under magnetic field. However,

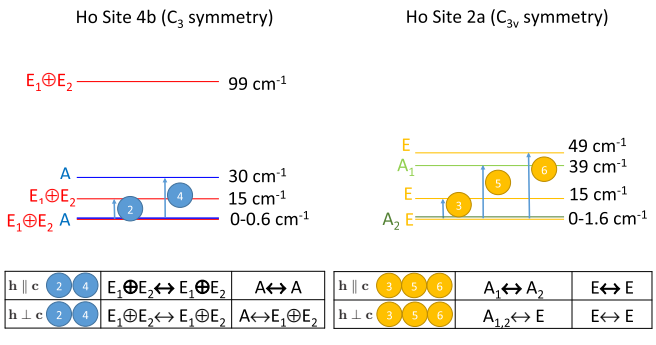

FIG. 5. Crystal-field scheme and selection rules of the parameter set 1 for the two different holmium sites with a tentative matching of the calculated CF transitions with the observed THz bands: Two transitions are expected for site 4*b* corresponding to band 2 and 3 and three for site 2*a* corresponding to bands 4, 5, and 6. The selection rules and the symmetry of the levels are indicated below.

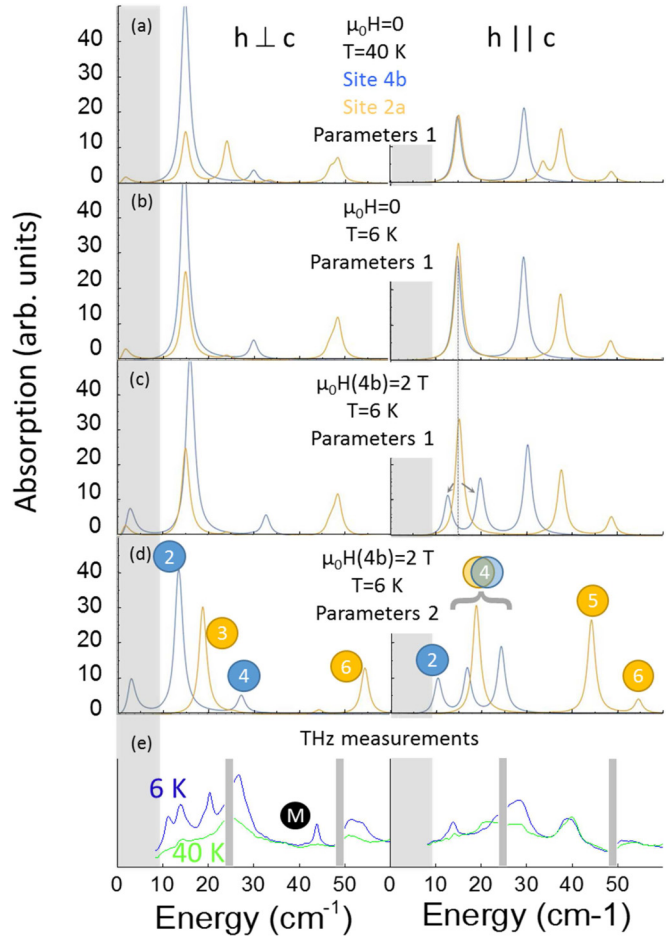

FIG. 6. (a)–(d) Calculated CF THz absorption spectra for both orientations of the THz magnetic field **h** and for Ho sites 4*b* (blue) and 2*a* (yellow), using parameter set 1 at 40 K, and zero magnetic field (a) at 6 K and (b) at 6 K with a 2 T magnetic field parallel to the *c*-axis. The dashed line and the two gray arrows for **h** ∥ **c** indicate the splitting of the lowest energy Ho 4*b* CF excitation under a magnetic field. Panel (d) corresponds to the calculations performed using the parameter set 2 at 6 K and under a magnetic field of 2 T along the *c*-axis with a tentative matching of the calculations with the measured bands of excitations. (e) Measured THz spectra at 40 and 6 K for comparison.

experimentally, there are abrupt changes at T_{SR} for all the THz bands, both on their position and their intensity, which cannot be accounted for by the sole effects of temperature and molecular field. This is a strong indication that electric effects with modification of electric charge screening of the oxygen ions are at play at T_{SR}. This is further corroborated by the observation simultaneously of a sharp anomaly in the dielectric constant as well as a jump in the electric polarization along the *c*-axis [31].

With little additional changes of some CF parameters (set 2 in Table I), we can reproduce qualitatively most of the observed features in the THz spectra [see Fig. 6(d) for T = 6 K and a field of 2 T]. In particular, bands 2, 3, 4, 5, and 6 are predicted at energies closer to the measured ones, although there are still some discrepancies with the calculated intensities. The presence of peak 3 above T_{SR} for **h** ∥ **c** and its

disappearance below T_{SR} while a new peak labeled 2 appears at lower energy could be due to the field splitting ascribed to the Ho-Mn coupling. Band 4 for $\mathbf{h} \parallel \mathbf{c}$ below T_{SR} could then result from a mixture of several peaks including the higher-energy mode from the split peak [see the horizontal bracket in Fig. 6(d)].

Strikingly, for $\mathbf{h} \perp \mathbf{c}$, band 1 appearing at T_{SR} in the measurements is missing in the calculations and therefore cannot be accounted for by the effect of a magnetic field. This discrepancy between calculations and experiment is another indication that hybridization is at play between Ho CF excitations and the lowest-energy Mn magnon (M').

VI. DISCUSSION

Our analysis and calculations for the Mn magnetic order and associated spin waves, using the spin Hamiltonian of Eq. (A1) in the Appendix A 1, can account for most of the experimental data. Mainly, two spin branches M and M' are observed with INS that are correctly calculated (Figs. 2 and 8). In particular, the spin reorientation at T_{SR} is clearly seen as a change in the spin-wave dispersion along $\mathbf{c}^*$ for the branch M' and is correctly captured when the change of Mn spin configuration from Γ_4 to Γ_3 is introduced. The second branch M is also observed with THz spectroscopy (Fig. 5), in agreement with the model. As for the nondispersive Ho CF excitations observed with INS and THz spectroscopy, our calculations using the CF Hamiltonian described by Eqs. (2) and (3) are able to reproduce the experimental data qualitatively when two ingredients are included: first, a change in charge screening at T_{SR} that explains the observed shifts and changes in intensity of the whole CF spectrum, and second, a molecular field along the c-axis produced by the Mn order. Similarly, a molecular field produced by the Ho 4b order may be introduced to account for the increased anisotropy gap in the Mn spin-wave branch M'. However, our calculations do not agree quantitatively with all the experimental data: they cannot describe properly how the Mn spin branch M' becomes nondispersive along $(1, 0, \ell)$ and seems to merge into Ho CF excitations below 20 K. Moreover, they cannot explain the THz band 1 that appears at T_{SR} and is locked at 3 cm^{-1} below band 2 (Fig. 4). Additional ingredients should be at play there that couple, for instance, the 3d and 4f magnetic species dynamically.

It is possible for Mn magnons and Ho crystal-field excitations to hybridize if they are close in energy, which is the case for $HoMnO_3$, where six different Ho crystal-field excitations lie in the energy range of the Mn spin waves (see Fig. 3). These hybridization processes also should not be forbidden by symmetry. This can be checked using a group representation analysis for both the Mn spin waves and the Ho crystal-field excitations: if they contain at least one common irreducible representation, the coupling is allowed. The details of our analysis are given in Appendix A 4. From this, we conclude that, in the energy range relevant for the experimental data reported in this study, all the CF excitations except one (band 5 associated with Ho 2a) are allowed to couple to Mn spin waves. Looking back at neutron experiments and the spin-wave calculations reproduced in Fig. 7, it can be seen that, when the temperature is lowered close to T_{SR}, the magnon

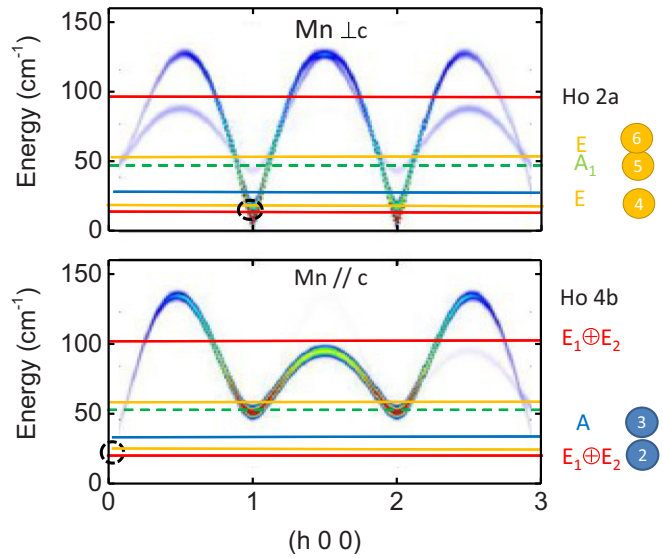

FIG. 7. (a) Mn spin-wave calculations along $(h, 0, 0)$ for spin fluctuations within the ab-plane (upper panel) and along the c-axis (lower panel). The calculated CF levels are added for the Ho 4b site (red and blue lines) as well as the Ho 2a site (yellow and green lines). The coupling of these CF excitations with the Mn magnons is always allowed by symmetry for all but the dashed line.

M' with small gaps at the zone centers (1,0,0) and (1,0,1) becomes close in energy to Ho (4b) CF excitations (bands 2 and 3–4), with different spectral weight for the magnons depending on the magnetic order Γ_3 or Γ_4. A coupling mechanism may be at play here that contributes to the spin reorientation process and the loss of dispersion for M' along $\mathbf{c}^*$.

Additionally, the 2 T effective magnetic field experienced by the 4b Ho suggests a coupling strength $g \sim 0.1$ K. In this context, and given the neutron-scattering data and the CF analysis detailed above, we may want to consider a possible dynamical coupling between (i) in-plane Mn spin-wave modes with Ho CF transitions polarized along the c-axis, and (ii) out-of-plane Mn spin-wave modes with Ho CF transitions polarized in the (a, b) plane. In this view, it is tempting to assign band 1 to the Mn spin-wave M' hybridized with CF band 2 (and also likely with band 3). In this scenario, the in-plane character of the CF transitions would be transferred to the hybrid mode, which would now appear in the $\mathbf{h} \perp \mathbf{c}$ channel as observed experimentally in the THz measurements, instead of the expected $\mathbf{h} \parallel \mathbf{c}$ channel expected for a nonhybridized M mode. This hybridization occurs only below T_{SR} when the spectral weight of these excitations is enhanced and their energy matches. The energy difference between bands 1 and 2, around 3 cm^{-1} experimentally, is in agreement with the coupling strength g when all the Ho-Mn links are considered (12 of them). Further calculations of the Mn spin waves are required where this coupling term is included.

VII. CONCLUSION

To summarize, we have reexamined the THz dynamics present in the multiferroic compound $HoMnO_3$. The

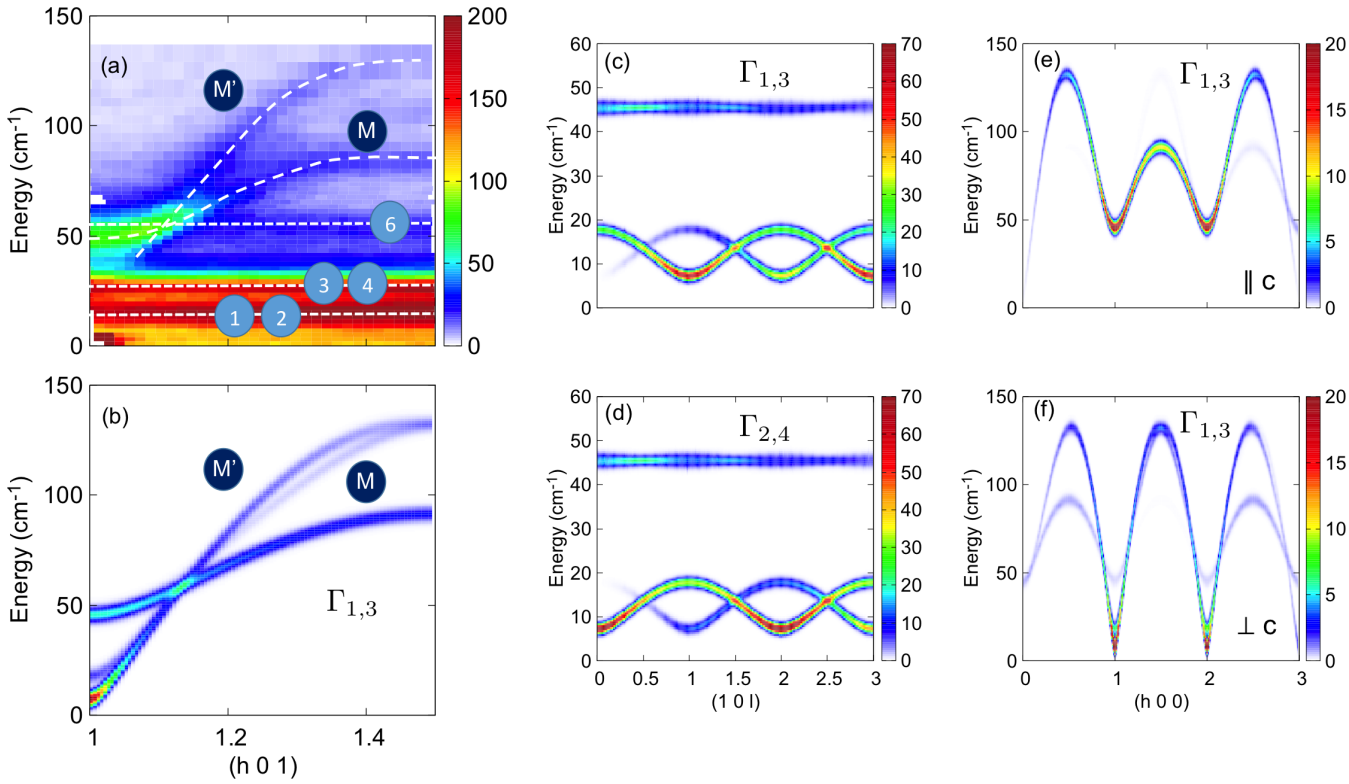

FIG. 8. Spin dynamics in $HoMnO_3$. (a) Mn^{3+} spin waves and Ho^{3+} CF excitations measured by INS along the $(h, 0, 1)$ reciprocal space direction. These data have been taken on IN8 at 2 K with a medium energy resolution of about 0.8 meV. M and M' denote the Mn dispersive spin waves that can be seen at the zone center. Labels 1–6 refer to nondispersive Ho CF lines. (b) Comparison with spin-wave calculations using the model described in the text for the $\Gamma_{1,3}$ configurations of the Mn magnetic structure. The following values of the parameters have been used: $J = 2.5$ meV, $D_z = 0.65$ meV, $K_1 = 0.005$ meV, $K_2 = 0.008$ meV, and $D_x = D_y = 0.0025$ meV. (c),(d) Spin-wave calculations along $(1, 0, \ell)$ for the four different possible Γ_i (among which are two homometric pairs with $x_{Mn} = 1/3$). The calculations were performed with the same parameters for the Hamiltonian as for panel (b) except for the hierarchy of K_1 and K_2 on the one hand and D_x and D_y on the other hand according to Table II. (e,f) Spin-wave calculations along $(h, 0, 0)$ in the $\Gamma_{1,3}$ configurations for spin fluctuations, respectively, along the c-axis (e) and within the basal hexagonal plane (f). The color vertical bars give the neutron counts in arbitrary units for all the panels. All the spin-wave calculations have been performed using the SPINWAVE software [45]. Note that in all the calculations of panels (b)–(f), modest but finite values of D_x and D_y were taken into account to ensure the stability of the various Γ_i; see Table II. This is responsible for the rise of the small gaps at the zone centers.

peculiarity of this Ho compound in the hexagonal manganites is the occurrence of a spin reorientation below $T_{SR} = 37$ K. Remarkably, several Ho CF excitations are present in the same energy range as the Mn spin waves. Thanks to the complementary neutron and electromagnetic wave probes, we have identified five Ho 4*b* and Ho 2*a* CF excitations, and we showed how Mn spin waves as well as Ho CF are affected by the reorientation process at T_{SR}. Using spin-wave and CF calculations, we are able to reproduce qualitatively most of the observed features. At T_{SR}, the Mn spin configuration switches from the high-temperature Γ_4 configuration to Γ_3. A change in the spectral weight is observed along the $(1, 0, \ell)$ direction that is correctly calculated in a simple Hamiltonian for the Mn spin waves. At the same time, changes occur in the CF excitations that can be accounted for when coupling to the surrounding oxygen charges is introduced. Then, Ho CF excitations start to match in energy the Mn branch at different Brillouin-zone centers. Further inspection of the neutron and THz data points toward additional Ho-Mn coupling mechanisms that show up below T_{SR} in two different ways: first as an additional excitation observed in THz spectroscopy that is locked 3 cm^{-1} below a CF excitation, and secondly the progressive disappearance of the Mn dispersion along $\mathbf{c}^*$. Our detailed study on $HoMnO_3$gives finally new insight into the very rich rare-earth–transition-metal dynamical couplings that show up in the THz range.

ACKNOWLEDGMENT

This work was financially supported by the NR-13-BS04-0013.

APPENDIX

1. Neutron scattering

A number of inelastic neutron-scattering studies have been reported on the magnetic excitations for several members of the $RMnO_3$ family [13,20,23,34–38]. Figure 8(a) gives an overview of the results obtained for $HoMnO_3$ in the present work. It shows the spectra along $\mathbf{a}^*$ and along $\mathbf{c}^*$. Dispersive spin waves are clearly visible along $\mathbf{a}^*$ with a maximum of the branches around 17 meV (140 cm^{-1}) while the amplitude

TABLE II. Condition for the Mn^{3+} single-ion anisotropy and the interplane couplings stabilizing one three-dimensional magnetic order of the Mn out of the four irreducible representations Γ_i.

Γ_i	ϕ	$\Delta\phi$	Conditions
1	$\pi/2$	π	$D_y \geqslant D_x, K_1 - K_2 \geqslant 0$
2	0	π	$D_y \leqslant D_x, K_1 - K_2 \geqslant 0$
3	0	0	$D_y \leqslant D_x, K_1 - K_2 \leqslant 0$
4	$\pi/2$	0	$D_y \geqslant D_x, K_1 - K_2 \leqslant 0$

of the dispersion along $\mathbf{c}^*$ is much weaker, reflecting the hierarchy of the magnetic interactions much stronger within the *ab*-planes than in between them. In addition to the spin waves, nondispersive excitations are visible corresponding to transition between CF levels of the two Ho^{3+} ions on 4*b* and 2*a* sites.

The relevant Hamiltonian to describe the Mn spin waves reads

$$\mathcal{H} = \frac{1}{2}\sum_{p,\langle i,j\rangle} J_{i,j}\mathbf{S}_{i,p}\mathbf{S}_{j,p} + \frac{1}{2}\sum_{\langle i,j\rangle} K_{i,j}\mathbf{S}_{i,1}\mathbf{S}_{j,2} + \sum_{i,p} D_z(\mathbf{S}^z_{i,p})^2 - D_x(\mathbf{S}^x_{i,p})^2 - D_y(\mathbf{S}^y_{i,p})^2. \quad \text{(A1)}$$

In this expression, $\mathbf{S}_{i,p}$ is the Mn spin at site i ($S = 2$), $p = 1, 2$ is an index that labels the two Mn planes (with $z = 0$ and $z = 1/2$) in the unit cell, D_z is an easy plane anisotropy ($D_z \geqslant 0$), and $D_{x,y} \geqslant 0$ are effective easy axis anisotropies, forcing the spins to point along the x or y directions (see Fig. 1). $J_{i,j} = J$ is the antiferromagnetic coupling between neighboring spins in the same plane, and $K_{i,j}$ the antiferromagnetic coupling between neighboring spins in adjacent planes. As shown in Fig. 1(a), the x_{Mn} position allows us to distinguish two different paths for K, a long and a short one,labeled hereafter as K_1 and K_2.

To proceed, we first assume $D_x = 0$ and $D_y = 0$. Straightforward classical minimization of $\mathcal{H}$ shows that the ground-state structures are planar 120° spin configurations. Using the convention of Fig. 1, the moments are given by

$$\mathbf{S}_{i,p} = S\begin{pmatrix}\cos\left[\phi_p + (i-1)\frac{2\pi}{3}\right]\\ \sin\left[\phi_p + (i-1)\frac{2\pi}{3}\right]\\ 0\end{pmatrix} \quad \text{(A2)}$$

and the classical energy reads

$$\mathcal{E} = -3JS^2 + 2(K_1 - K_2)S^2\cos\Delta\phi \;\text{ with } \Delta\phi = \phi_2 - \phi_1. \quad \text{(A3)}$$

The value of ϕ_1 along with the relative phase difference $\Delta\phi = \phi_2 - \phi_1$ between two adjacent planes fully determine the final structure. These structures can be classified using the $\Gamma_{i=1,2,3,4}$ irreducible representations listed in Table II. Note that two two-dimensional irreducible representations are also allowed in the $P6_3cm$ space group but were not considered in this work since they were discarded in previous studies. The sign of $K_1 - K_2$ determines the stability of each phase: $\Gamma_{1,2}$ are stabilized for $K_1 - K_2 \geqslant 0$, while $\Gamma_{3,4}$ are stabilized for $K_1 - K_2 \leqslant 0$.

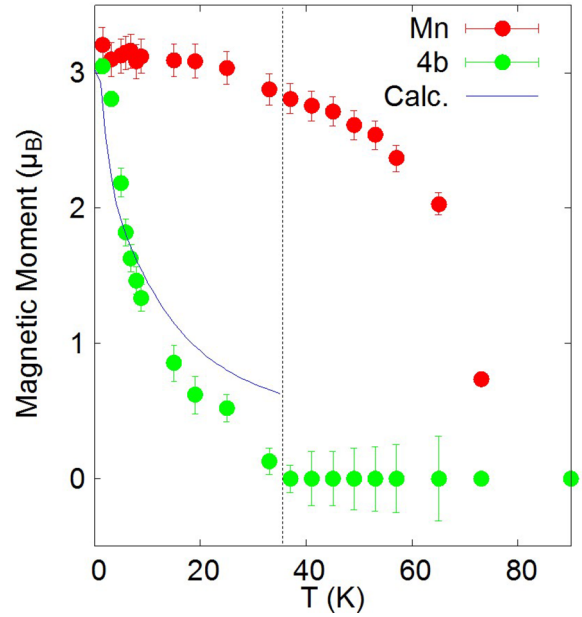

FIG. 9. Temperature dependence of the ordered magnetic moments Ho 4*b* extracted from the refinement of the neutron-diffraction data (green dots) compared to the calculated magnetic moment (blue line) induced by a constant magnetic field of 2 T due to the coupling with the Mn magnetism. The red dots show the Mn ordered moment also extracted from the neutron-diffraction data.

In principle, six spin-wave branches are expected in this model. However, since $K_1 \approx K_2$, these branches should be considered as three almost doubly degenerate modes. Moreover, due to the hexagonal symmetry, these three branches can be described by a single one, stemming from $(0, 0, \ell)$ and going soft at $(3, 0, \ell)$. The two other branches are identical but stem from $(1, 0, \ell)$ and $(2, 0, \ell)$ and go soft, respectively,

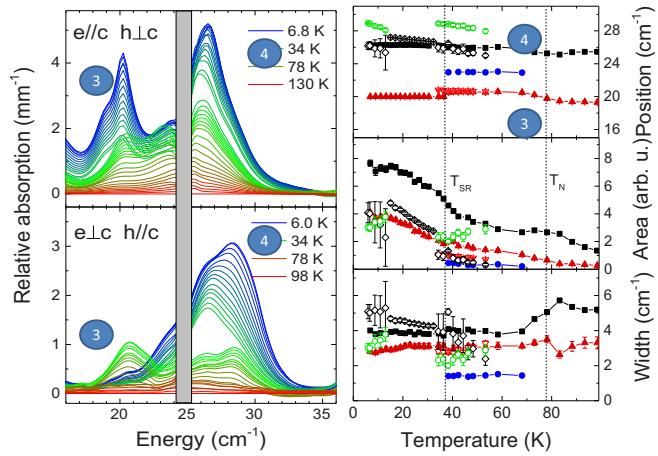

FIG. 10. Details of the THz spectra around bands 3 and 4. Left: relative absorption measured for two different orientations of **e** and **h** on the same sample. Right: results of Gaussian fits for the absorption peaks with the position, area, and width as a function of temperature. A maximum of three peaks was used. Closed and open symbols refer to $\mathbf{h} \perp \mathbf{c}$ and $\mathbf{h} \parallel \mathbf{c}$, respectively. Note the complexity of the spectra with several components that are all affected by T_{SR}.

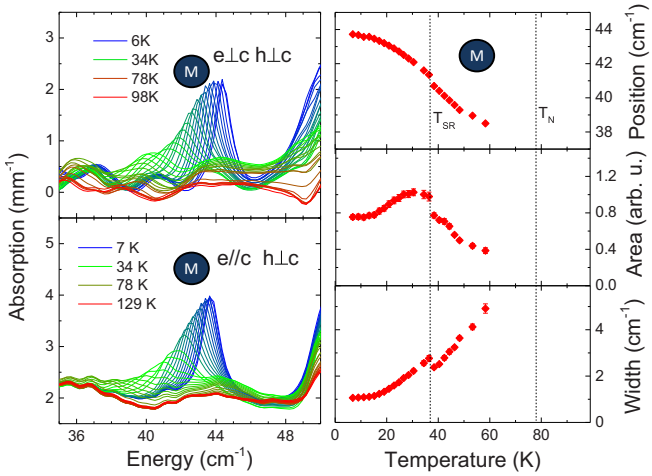

FIG. 11. Details of the THz spectra around the magnon excited for a THz **h** field perpendicular to the *c*-axis. Left: Absorption measured at different temperatures for two different directions of the THz **e** field on two different samples. Right: results of the Gaussian fits of the absorption peak with the position, area, and width as a function of temperature obtained for **e** ∥ **c** (with similar results for **e** ⊥ **c**). Note the emergence of the magnon *M* below T_N and how it is affected by T_{SR}.

at $(4, 0, \ell)$ and $(5, 0, \ell)$. As shown in Figs. 8(c) and 8(d), spin-wave calculations indicate that the former corresponds mostly to correlations between spin components along the *c*-axis [Fig. 8(c)], while the two latter correspond mostly to in-plane correlations [Fig. 8(d)]. As a result, two acoustic-like spin waves and one optical-like spin wave emerge from each zone center. The gap Δ of the latter occurs at around 45 cm^{-1}

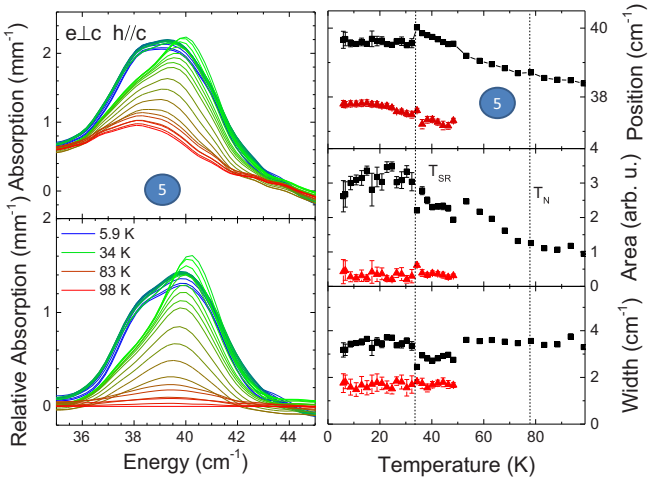

FIG. 12. Details of the THz spectra around band 5 when **h** ∥ **c**. Left: absolute and relative absorption measured at different temperatures. Right: results of Gaussian fits for the absorption peaks with the position, area, and width as a function of temperature. Two peaks are present. The lower-energy peak appears smoothly when lowering the temperature and can be fitted below 50 K. The higher-energy one, the stronger, is affected at T_{SR} with a small shift in energy and increased width and area.

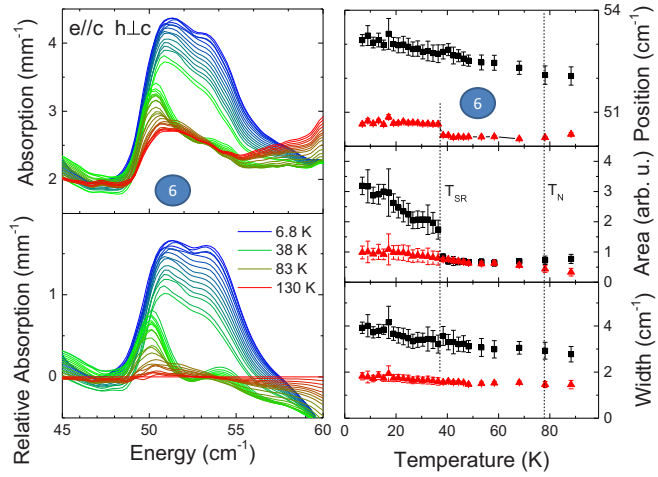

FIG. 13. Details of the THz spectra around band 6 when **h** ⊥ **c**. Left: absolute and relative absorption measured at different temperatures. Right: results of Gaussian fits for the absorption peaks with the position, area, and width as a function of temperature. Two peaks are present that are both affected at T_{SR}.

(5 meV) and is related to the easy-plane anisotropy by $\Delta \approx 3S\sqrt{D_z J}$.

As explained above, the degeneracy is lifted as soon as $K_1 \neq K_2$. This becomes especially clear when looking at the dispersion along $(1, 0, \ell)$. This point is illustrated in Figs. 8(e) and 8(f), showing the calculated spin-wave dispersions for the different Γ_i magnetic configurations. We notice that the spectral weight of the lowest energy mode is strong at (1,0,1) for $\Gamma_{1,3}$, and at (1,0,0) in the case of $\Gamma_{2,4}$. This change has been put forward in Ref. [20] to explain that the spin reorientation process in $HoMnO_3$ involves a symmetry change from $\Gamma_{2,4}$ below T_N to $\Gamma_{1,3}$ below T_{SR}. This change was attributed to a change of sign of $K_1 - K_2$ induced by the change in position of the Mn ions from $x_{Mn} = 0.325$ above T_{SR} to $x_{Mn} \approx 0.334$ below. In Ref. [20], the authors assumed Γ_1 to be the ground state. Actually, nonlinear optical measurements as well as other probes suggest rather a Γ_3 magnetic order below T_{SR} [27,28,30]. Since the $\Gamma_{1,3}$ and $\Gamma_{2,4}$ pairs are homometric, i.e., they cannot be distinguished by unpolarized neutron

TABLE III. Peak positions deduced from THz spectroscopy and neutron-diffraction measurements at the (1,0,0) reciprocal space position.

		THz		Neutron	
Band	Selection rule	45 K	27 K	45 K	27 K
M'					6 cm^{-1}
M	**h** ⊥ **c**	39.9 cm^{-1}	42.5 cm^{-1}	41 cm^{-1}	45 cm^{-1}
1	**h** ⊥ **c** only		11.1 cm^{-1}		11 cm^{-1}
2	**h** ⊥ **c** and **h** ∥ **c**	14.3 cm^{-1}	13.6 cm^{-1}	14 cm^{-1}	13 cm^{-1}
3	**h** ⊥ **c** and **h** ∥ **c**	20.6 cm^{-1}	20.1 cm^{-1}	21 cm^{-1}	20 cm^{-1}
4	**h** ⊥ **c** and **h** ∥ **c**	25.9 cm^{-1}	26.8 cm^{-1}	25 cm^{-1}	26 cm^{-1}
5	**h** ∥ **c** mainly	39.6 cm^{-1}	39.5 cm^{-1}		
5	**h** ∥ **c** mainly	37.2 cm^{-1}	37.6 cm^{-1}		
6	**h** ∥ **c** mainly	52.6 cm^{-1}	52.9 cm^{-1}		
6	**h** ∥ **c** mainly	50.2 cm^{-1}	50.7 cm^{-1}		

TABLE IV. C_3 (3) character table.

C_3	3	1	3^+	3^-	Functions
A	Γ_1	1	1	1	z, x^2+y^2, J_z
E_2	Γ_2	1	ω^2	ω	
					$x, y, xz, yz, x^2-y^2, xy, J_x, J_y$
E_1	Γ_3	1	ω	ω^2	

scattering if x_{Mn} is strictly equal to 1/3, we have assumed that Γ_3 is the actual ground state in the present work.

In the Ho CF calculations, we introduce a constant magnetic field to simulate the effect of the Ho-Mn coupling. We used the measured Ho 4*b* and Mn ordered moment extracted from neutron-diffraction data [39]: Ho 4*b* moments are observed along the *c*-axis; a molecular field of 2 T along this direction is able to polarize Ho spins with the correct magnitude and temperature dependence at least below 10 K (see Fig. 9). The Mn moment varies only slightly below T_{SR}, thus validating the assumption of a constant molecular field. Such a field corresponds to a coupling strength $g \sim 0.1$ K in Eq. (1) when the six neighbors and the spin values are used.

2. THz spectroscopy

A detailed representation of the THz spectra is given in Figs. 4 and 10–13 for the different bands, labeled 1–6, and the Mn magnon *M*. The parameters of the Gaussian fits used for the absorption peaks are also reported. The changes occurring at the reorientation transition T_{SR} were already mentioned earlier for bands 1 and 2, but they are also visible for the other excitations: band 3, always present for $\mathbf{h} \perp \mathbf{c}$, disappears below T_{SR} when $\mathbf{h} \parallel \mathbf{c}$, while band 4 has a strong increase below T_{SR} (see Fig. 10). Note that band 3 below T_{SR} might have a shoulder and that band 4 encompasses certainly several modes. Finally, band 6 (and maybe also band 5) has a side band that increases below T_{SR} (see Figs. 12 and 13). The Mn magnon (*M*) is also affected by the spin reorientation at T_{SR}: an abrupt change, although weak, occurs in its position and linewidth, while its area, which was increasing below T_N, starts to decrease and becomes temperature-independent below 10 K (see Fig. 11). A summary of the peak positions and selection rules is given in Table III together with those obtained from the neutron measurements.

3. Symmetry analysis: THz spectroscopy selection rules for CF excitations

The THz wave interacts with the sample through its electric field (a polar vector) and magnetic field (an axial vector). The eigenstates of the crystal-field Hamiltonian transform under the symmetry element according to one of the irreducible representations of the site symmetry group. On the other hand, a polar (axial) vector transforms according to the D_1^- (D_1^+) irreducible representation of the rotation group O(3). It reduces to $D_1^- = A \bigoplus E_1 \bigoplus E_2$ ($D_1^+ = A \bigoplus E_1 \bigoplus E_2$) with respect to the irreducible representation of the site 4*b* point group C_3 and $D_1^- = A_1 \bigoplus E$ ($D_1^+ = A_2 \bigoplus E$) with respect to the irreducible representation of the site 2*a* point group C_{3v}, as can be seen from Tables 4 and 5. The selection rules follow from the theorem of three representations, which allow us to state that the matrix elements of the electric (magnetic) transition between two eigenstates is nonzero solely if the reduction of the tensor product of the representation associated with the initial state and that of a polar (axial) vector contains the representation associated with the final state. The deduced THz selection rules can then be derived for Ho 4*b* and 3*b* CF excitations. They are reported in Fig. 5.

TABLE V. C_{3v} (3) character table.

C_{3v}	$3m$	1	3	m	Functions
Multiplicity		1	2	3	
A_1	Γ_1	1	1	1	z, x^2+y^2, z^2
A_2	Γ_2	1	1	-1	J_z
E	Γ_3	2	-1	0	$x, y, xz, yz, x^2-y^2, xy, J_x, J_y$

TABLE VI. C_{6v} (6*mm*) character table.

C_{6v}	6*mm*	1	2	3	6	m_d	m_v	Functions
Multiplicity		1	1	2	2	3	3	
A_1	Γ_1	1	1	1	1	1	1	z, x^2+y^2, z^2
A_2	Γ_2	1	1	1	1	-1	-1	J_z
B_1	Γ_3	1	-1	1	-1	1	-1	
B_2	Γ_4	1	-1	1	-1	-1	1	
E_2	Γ_5	2	2	-1	-1	0	0	z, x^2-y^2, xy
E_1	Γ_6	2	-2	-1	1	0	0	$x, y, xz, yz\ J_x, J_y$

4. Symmetry analysis: Ho-Mn coupling

For Mn magnons and Ho crystal-field excitations to hybridize, the symmetry requirements can be derived through a group representation analysis for the Mn spin waves and the Ho crystal-field excitations. The Mn order with zero propagation vector is described by the isomorphic space group C_{6v}^3. The Mn spin-wave representations can be reduced to representations of the associated point group C_{6v} (6*mm*). This group contains the lower symmetric C_3 (3) and C_{3v} (3*m*) that best describe the Ho CF schemes. In the present analysis, to look at possible coupling mechanisms with the Mn spin waves, we will rewrite the CF representations in the more symmetric C_{6v}. Its character table is given in Table 6.

The symmetry of the different Mn spin waves has been reported in [46] with Kovalev notation. We will use Mulliken notation instead. To simplify the calculations, the spin-wave analysis has been performed in a more symmetric space group than C_{6v}^3, namely D_{6h}^4, which means neglecting some oxygen displacements and therefore some weak magnetic anisotropies. From [46], it follows that the spin-wave representation can be decomposed into $A_{2g} \bigoplus B_{1g} \bigoplus E_{1g} \bigoplus E_{2g}$. Going back to the lower symmetric C_{6v}^3 space group, gerade and ungerade modes are no longer relevant so that the spin-wave decomposition becomes $A_2 \bigoplus B_1 \bigoplus E_1 \bigoplus E_2$. When spin anisotropies are introduced, the degeneracy of the low-energy branches is lifted, as can be seen in our spin-wave calculations (Fig. 8), dictating the use of magnetic Shubnikov groups.

TABLE VII. Correlations between the global frame point group C_{6v} (6*mm*) and the two local frame point groups C_3 (3) and C_{3v} (3*m*).

C_{6v}	C_3	C_{3v}
6mm	3	3m
A_1	A	A_1
A_2	A	A_2
B_1	A	A_2
B_2	A	A_1
E_2	E_1, E_2	E
E_1	E_1, E_2	E

For Ho CF schemes, the character tables for the associated point groups C_3 (3) and C_{3v} (3*m*) are reported in Tables 4 and 5. Their correlations to the more symmetric C_{6v} group that we will use are given in Table 7. For Ho 4*b*, in its local C_3 symmetry, two different kinds of symmetry are present for the crystal-field states: singlets are described by the irreducible representation A and degenerate doublets are described by $E_1 \bigoplus E_2$. These irreducible representations induce, in the higher symmetric C_{6v} group, states that are decomposed into linear combinations of $\{A_1, A_2, B_1, B_2\}$ for the singlets and $\{E_1, E_2\}$ for the degenerate doublets. For the Ho 2*a*, in the local C_{3v} symmetry, three different symmetries are present: singlets A_1 and A_2, and doublets E. They induce, in C_{6v} symmetry, states that are decomposed into $\{A_1, B_2\}$ and $\{A_2, B_1\}$, respectively, for the singlets and $\{E_1, E_2\}$ for the doublets.

From these considerations, we can now look at possible coupling between the Mn spin waves and the Ho 4*b* and 2*a* crystal-field excitations that are allowed by symmetry, that is, if their representations contain at least one common irreducible representation. This is the case for all CF excitations except for the Ho 2*a* A_1 singlets.

All the tables reproduced here were established thanks to [47].

[1] A. Pimenov, A. A. Mukhin, V. Yu. Ivanov, V. D. Travkin, A. M. Balbashov, and A. Loidl, Nat. Phys. **2**, 97 (2006).

[2] A. B. Sushkov, R. V. Aguilar, S. Park, S.-W. Cheong, and H. D. Drew, Phys. Rev. Lett. **98**, 027202 (2007).

[3] N. Kida, D. Okuyama, S. Ishiwata, Y. Taguchi, R. Shimano, K. Iwasa, T. Arima, and Y. Tokura, Phys. Rev. B **80**, 220406(R) (2009).

[4] S. P. P. Jones, S. M. Gaw, K. I. Doig, D. Prabhakaran, E. M. Hétroy Wheeler, A. T. Boothroyd, and J. Lloyd-Hughes, Nat. Commun. **5**, 3787 (2014).

[5] H. Katsura, A. V. Balatsky, and N. Nagaosa, Phys. Rev. Lett. **98**, 027203 (2007).

[6] T. H. Arima, J. Phys. Soc. Jpn. **76**, 073702 (2007).

[7] M. Mochizuki, N. Furukawa, and N. Nagaosa, Phys. Rev. Lett. **105**, 037205 (2010).

[8] M. Mochizuki, N. Furukawa, and N. Nagaosa, Phys. Rev. Lett. **104**, 177206 (2010).

[9] L. Chaix, S. de Brion, F. Lévy-Bertrand, V. Simonet, R. Ballou, B. Canals, P. Lejay, J. B. Brubach, G. Creff, F. Willaert, P. Roy, and A. Cano, Phys. Rev. Lett. **110**, 157208 (2013).

[10] A. A. Sirenko, S. M. OMalley, K. H. Ahn, S. Park, G. L. Carr, and S.-W. Cheong, Phys. Rev. B **78**, 174405 (2008).

[11] T. D. Kang, E. Standard, K. H. Ahn, A. A. Sirenko, G. L. Carr, S. Park, Y. J. Choi, M. Ramazanoglu, V. Kiryukhin, and S.-W. Cheong, Phys. Rev. B **82**, 014414 (2010).

[12] L. Chaix, S. de Brion, S. Petit, R. Ballou, L.-P. Regnault, J. Ollivier, J.-B. Brubach, P. Roy, J. Debray, P. Lejay, A. Cano, E. Ressouche, and V. Simonet, Phys. Rev. Lett. **112**, 137201 (2014).

[13] S. Pailhès, X. Fabrèges, L. P. Régnault, L. Pinsard-Godart, I. Mirebeau, F. Moussa, M. Hennion, and S. Petit, Phys. Rev. B **79**, 134409 (2009).

[14] S. Tóth, B. Wehinger, K. Rolfs, T. Birol, U. Stuhr, H. Takatsu, K. Kimura, T. Kimura, H. M. Rønnow, and C. Rüegg, Nat. Commun. **7**, 13547 (2016).

[15] I. Aupiais, M. Mochizuki, H. Sakata, R. Grasset, Y. Gallais, A. Sacuto, and M. Cazayous, npj Quantum Mater. **3**, 60 (2018).

[16] E. F. Bertaut, F. Forrat, and P. Fang, C. R. Acad. Sci. (Paris) **256**, 1958 (1963).

[17] T. Katsufuji, M. Masaki, A. Machida, M. Moritomo, K. Kato, E. Nishibori, M. Takata, M. Sakata, K. Ohoyama, K. Kitazawa, and H. Takagi, Phys. Rev. B **66**, 134434 (2002).

[18] S. W. Cheong and M. Mostovoy, Nat. Mater. **6**, 13 (2007).

[19] H. Sim, J. Oh, J. Jeong, M. Duc Le, and J.-G. Park, Acta Crystallogr. Sect. B **72**, 3 (2016).

[20] X. Fabrèges, S. Petit, I. Mirebeau, S. Pailhès, L. Pinsard, A. Forget, M. T. Fernandez-Diaz, and F. Porcher, Phys. Rev. Lett. **103**, 067204 (2009).

[21] S. Lee, A. Pirogov, M. Kang, K.-H. Jang, M. Yonemura, T. Kamiyama, S.-W. Cheong, F. Gozzo, N. Shin, H. Kimura, Y. Noda, and J.-G. Park, Nature (London) **451**, 805 (2008).

[22] I. V. Solovyev and S. A. Nikolaev, Phys. Rev. B **90**, 184425 (2014).

[23] X. Fabrèges, I. Mirebeau, P. Bonville, S. Petit, G. Lebras-Jasmin, A. Forget, G. André, and S. Pailhès, Phys. Rev. B **78**, 214422 (2008).

[24] S. Chattopadhyay, V. Simonet, V. Skumryev, A. A. Mukhin, V. Y. Ivanov, M. I. Aroyo, D. Z. Dimitrov, M. Gospodinov, and E. Ressouche, Phys. Rev. B **98**, 134413 (2018).

[25] T. Lottermoser, T. Lonkai, U. Amann, D. Hohlwein, J. Ihringer, and M. Fiebig, Nature (London) **430**, 541 (2004).

[26] A. Munoz, J. A. Alonso, M. J. Martínez-Lope, M. T. Casáis, J. L. Martínez, and M. T. Fernández-Diaz, Chem. Mater. **13**, 1497 (2001).

[27] M. Fiebig, C. Degenhardt, and R. V. Pisarev, J. Appl. Phys. **91**, 8867 (2002).

[28] P. J. Brown and T. Chatterji, J. Phys.: Condens. Matter **18**, 10085 (2006).

[29] P. J. Brown and T. Chatterji, Phys. Rev. B **77**, 104407 (2008).

[30] S. Nandi, A. Kreyssig, L. Tan, J. W. Kim, J. Q. Yan, J. C. Lang, D. Haskel, R. J. McQueeney, and A. I. Goldman, Phys. Rev. Lett. **100**, 217201 (2008).

[31] N. Hur, I. K. Jeong, M. F. Hundley, S. B. Kim, and S.-W. Cheong, Phys. Rev. B **79**, 134120 (2009).

[32] D. Talbayev, A. D. LaForge, S. A. Trugman, N. Hur, A. J. Taylor, R. D. Averitt, and D. N. Basov, Phys. Rev. **101**, 247601 (2008).
[33] N. J. Laurita, Y. Luo, R. Hu, M. Wu, S. W. Cheong, O. Tchernyshyov, and N. P. Armitage, Phys. Rev. Lett. **119**, 227601 (2017).
[34] T. J. Sato, S.-H. Lee, T. Katsufuji, M. Masaki, S. Park, J. R. D. Copley, and H. Takagi, Phys. Rev. B **68**, 014432 (2003).
[35] J. Park, J.-G. Park, G. S. Jeon, H.-Y. Choi, C. Lee, W. Jo, R. Bewley, K. A. McEwen, and T. G. Perring, Phys. Rev. B **68**, 104426 (2003).
[36] O. P. Vajk, M. Kenzelmann, J. W. Lynn, S. B. Kim, and S.-W. Cheong, Phys. Rev. Lett. **94**, 087601 (2005).
[37] S. Petit, F. Moussa, M. Hennion, S. Pailhès, L. Pinsard-Gaudart, and A. Ivanov, Phys. Rev. Lett. **99**, 266604 (2007).
[38] T. Kim, J. C. Leiner, K. Park, J. Oh, H. Sim, K. Iida, K. Kamazawa, and J.-G. Park, Phys. Rev. B **97**, 201113(R) (2018).
[39] X. Fabrèges, Ph.D. thesis, Université Paris Sud-Paris XI (2010).
[40] S. G. Condran and M. L. Plumer, J. Phys.: Condens. Matter **22**, 162201 (2010).
[41] R. S. Fishman, J. A. Fernandez-Baca, and T. Rõõm, *Spin-Wave Theory and its Applications to Neutron Scattering and THz Spectroscopy* (IOP Publishing, Bristol, UK, 2018).
[42] P. Bowlan, S. A. Trugman, J. Bowlan, J.-X. Zhu, N. J. Hur, A. J. Taylor, D. A. Yarotski, and R. P. Prasankumar, Phys. Rev. B **94**, 100404(R) (2016).
[43] K. W. H. Stevens, Proc. R. Soc. London, Ser. A **65**, 209 (1952).
[44] M. T. Hutchings, in *Solid State Physics: Advances in Research and Applications*, edited by F. Seitz and B. Turnbull (Academic, New York, 1965), Vol. 16, p. 227.
[45] http://www-llb.cea.fr/logicielsllb/SpinWave/SW.html
[46] W. Sikora, O. V. Gurin, and V. N. Syromyatnikov, J. Magn. Magn. Mater. **71**, 225 (1988).
[47] M. I. Aroyo, A. Kirov, C. Capillas, J. M. Perez-Mato, and H. Wondratschek, Acta Crystallogr. A **62**, 115 (2006).